THE ASTROPHYSICAL JOURNAL, 425:707–719, 1994 April 20

A NEAR-INFRARED STUDY OF THE MONOCEROS R2 STAR FORMATION REGION

ERIC M. HOWARD, JUDITH L. PIPHER, AND WILLIAM J. FORREST
Department of Physics and Astronomy, University of Rochester, Rochester, NY 14627-0171
Received 1993 July 21; accepted 1993 October 28

ABSTRACT

We present H (1.65 μm), K (2.23 μm), and L' (3.81 μm) broad-band images as well as Brγ ($n = 7 \rightarrow 4$, 2.166 μm) and Brα ($n = 5 \rightarrow 4$, 4.052 μm) hydrogen recombination line images, and 3.29 μm and 3.4 μm unidentified feature emission images of the Monoceros R2 star formation region at a plate scale of $\sim 0\farcs9$ pixel^{-1}. The Brackett line images are combined with 5 GHz data to map the line-of-sight dust extinction to the compact H II region on a small spatial scale. This extinction map is then used to deredden regions of the H and K images interior to the H II region. IRS 1_{SW}, the ionizing source, is found to be consistent with a B0 star. Comparison of dereddened H and K images with the Brackett images and recent high-resolution HCO^+ measurements leads to the development of a torus model for the dense molecular gas surrounding the H II region. The 3.29 μm emission is found to be coincident with the ring of scattered light at 2.2 μm and just outside the Brα and Brγ emission. The 3.4 μm image is of too low a signal-to-noise ratio to determine if any variation in the 3.29 to 3.4 μm emission ratio with distance from the ionizing source is seen; however, 3.4 μm emission is detected in a ring coincident with the 3.29 μm emission.

Subject headings: dust, extinction — H II regions — infrared: ISM: continuum — infrared: ISM: lines and bands — ISM: individual (Monocerotis R2) — reflection nebulae — stars: formation

1. INTRODUCTION

Mon R2 is a reflection association described by van den Bergh (1966). Within Mon R2 is a region with many of the indicators of recent high-mass star formation including a compact H II region (Downes et al. 1975; Massi, Felli, & Simon 1985), H_2O and OH masers (Knapp & Brown 1976), and luminous compact near-infrared objects (Beckwith et al. 1976) with energy distributions suggestive of pre–main-sequence objects. IRS 1_{SW} (see Fig. 1) is thought to be the exciting source of the H II region. The luminous compact objects IRS 2 and IRS 3 are, most likely, pre–main-sequence objects. The region is also the site of a massive molecular outflow covering 28′ or 7.5 pc at a distance of 950 pc (Wolf, Lada, & Bally 1990). The dynamical timescale indicates that the Mon R2 flow is one of the oldest known outflows ($\sim 1.5 \times 10^5$ yr) (Wolf et al. 1990). The center of this outflow coincides with Mon R2 IRS, the 3′ region which is the subject of this paper.

Recent high spatial resolution K-band (2.2 μm) imaging and polarization measurements of the Mon R2 IRS have been reported by Aspin & Walther (1990). These measurements indicate the presence of polarization due to both scattering and dichroic absorption. Centrosymmetric polarization reaching 45% throughout a shell-like structure surrounding IRS 2 is strongly indicative of right-angle scattering. In the interior of the shell, polarization vectors reaching 10% in the same direction as the integrated polarization of IRS 2 are indicative of dichroic absorption due to a strong magnetic field or superparamagnetic grains. It is not known whether IRS 3 is located at the same distance along the line of sight as the H II region. It possesses a distinct centrosymmetric polarization pattern, indicating that it is not being illuminated by the same source as the shell structure surrounding IRS 2 (see Fig. 1 in Aspin & Walther 1991).

There has been some controversy on the degree of extinction and its variation toward the H II region in Mon R2 (see Natta et al. 1986). Since the estimates of the extinction cited in Natta et al. (1986) were deduced from observations in beams of varying size, large discrepancies in the estimates may result from small differences in pointing for nonuniform extinction. High spatial resolution imaging at several wavelengths is also needed to study the structure of the region, to determine the spatial variation of the color temperature of the emitting material, and to study the interaction of the embedded stars and/or young stellar objects (YSOs) with the surrounding gas and dust. IR colors of the various pointlike sources help determine which objects are foreground stars.

Measurements of Brα and Brγ line fluxes can yield an extinction estimate in two different ways. If a measurement of the optically thin radio flux density has been obtained for the same region, this radio flux density can be used to give a prediction of the intrinsic, unreddened Brα and Brγ line fluxes, for an assumed electron temperature (determined from the H109α radio recombination line; see Downes et al. 1975). Comparing the observed Bracket measurement with the predicted gives an extinction measure. If, on the other hand, an extinction law is assumed, the Brα-to-Brγ ratio can be used to give a direct estimate of the extinction (Herter 1981; Herter et al. 1981). Once the extinction to the ionized gas has been determined, this may be used to deredden the point sources and diffuse emission within the region (see § 4.2). We have obtained Brα and Brγ images of Mon R2 at high spatial resolution, along with broad-band H (1.65 μm), K (2.23 μm), and L' (3.81 μm) images to address these issues.

The broad-band emission has a diffuse component that includes a ring around IRS 1 and IRS 2 (the shell-like structure referred to earlier). The Brα and Brγ emission is found to be, for the most part, internal to this ring, with some overlap along the southeast edge. Gonatas, Palmer, & Novak (1992) have presented a high spatial resolution map of HCO^+ emis-

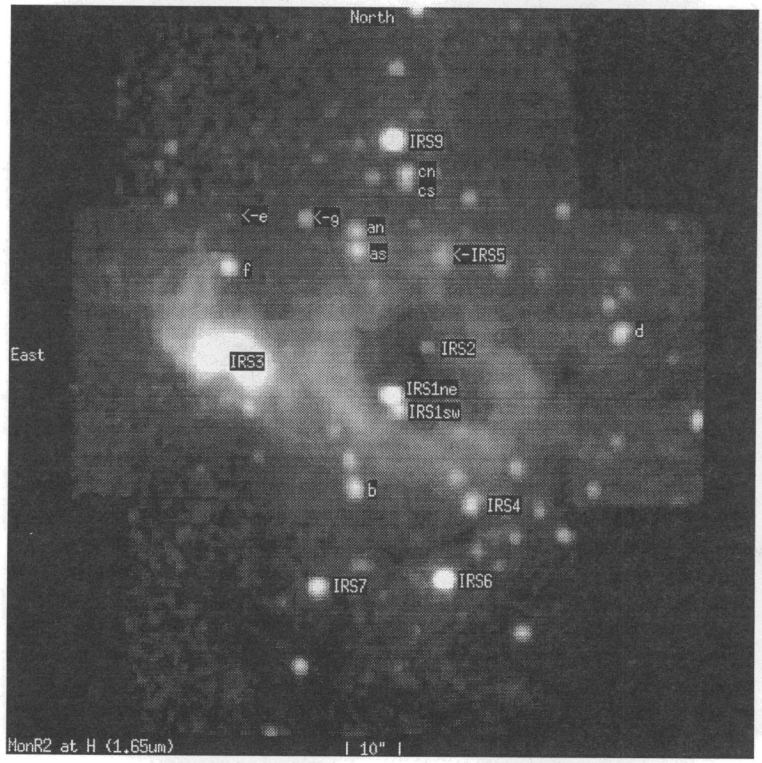

FIG. 1.—Mosaic of Mon R2 at H (1.65 μm), displayed on a square root scale

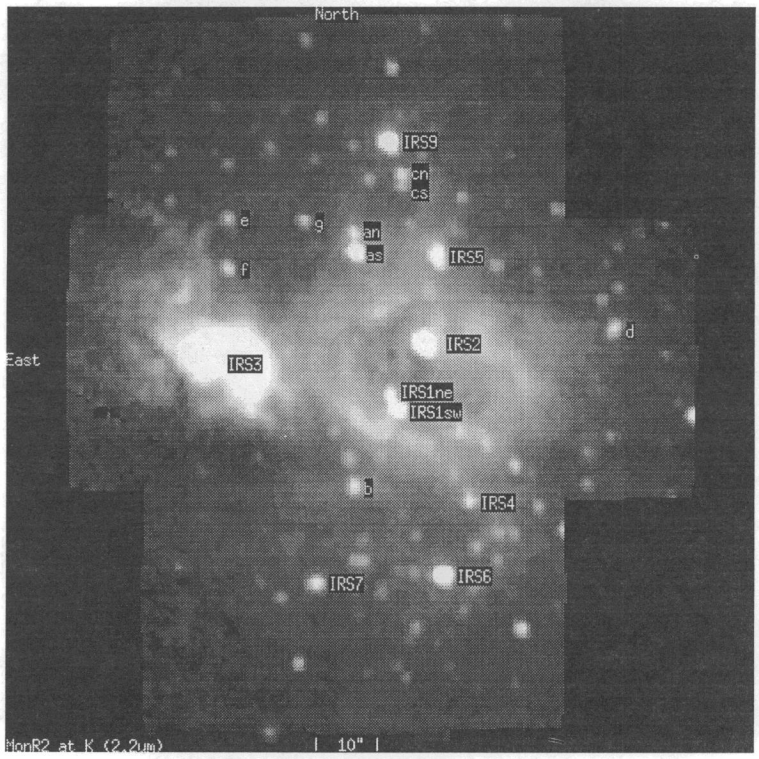

FIG. 2.—Mosaic of Mon R2 at K (2.23 μm), displayed on a square root scale

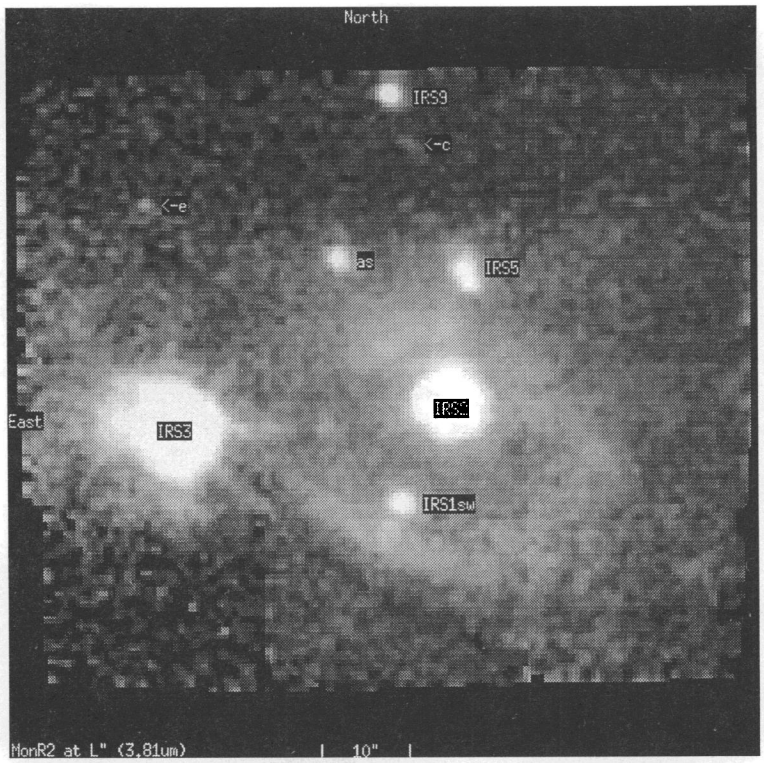

FIG. 3.—Mosaic of Mon R2 at L' (3.81 μm), displayed on a square root scale

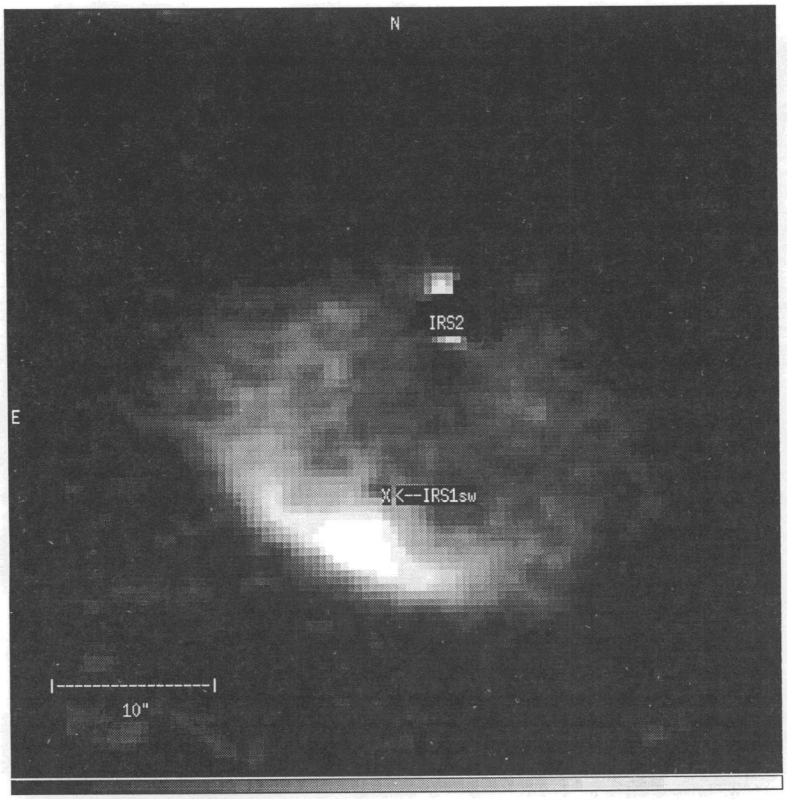

FIG. 4.—Brα ($n = 5 \rightarrow 4$, 4.052 μm) line minus continuum. Because of seeing variations, IRS 2 does not subtract well in any of the line minus continuum images.

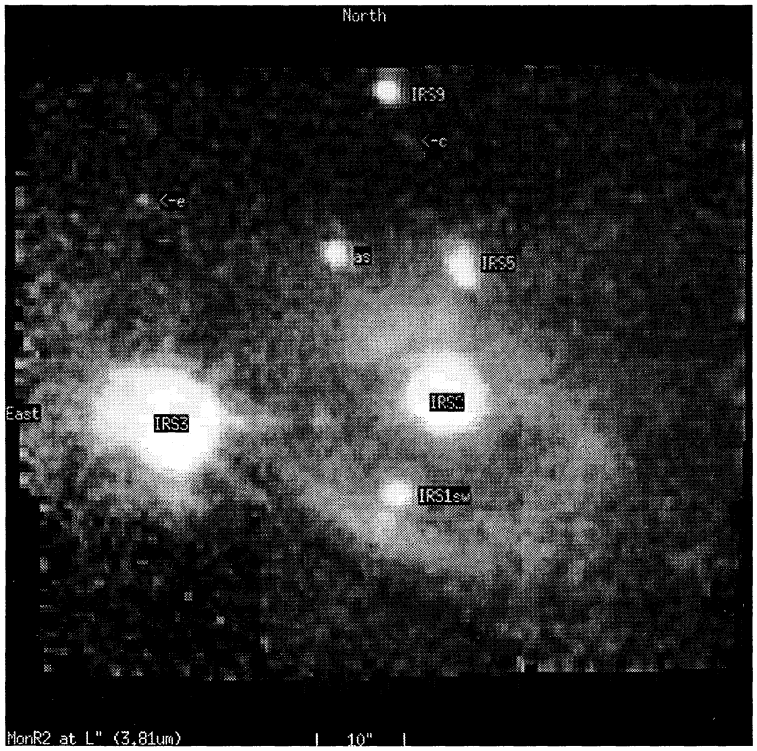

FIG. 3.—Mosaic of Mon R2 at L' (3.81 μm), displayed on a square root scale

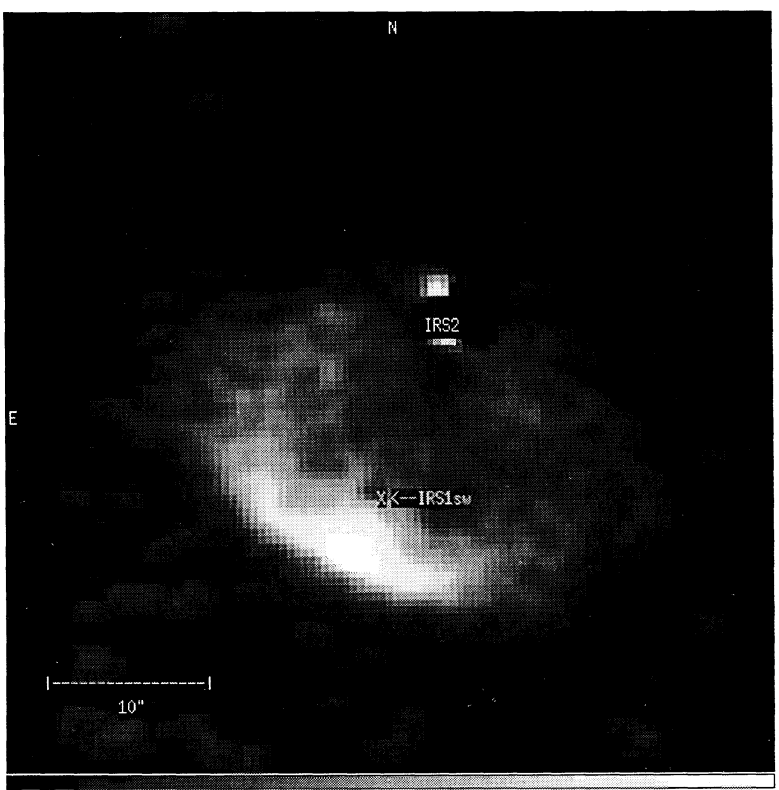

FIG. 4.—Brα ($n = 5 \rightarrow 4$, 4.052 μm) line minus continuum. Because of seeing variations, IRS 2 does not subtract well in any of the line minus continuum images.

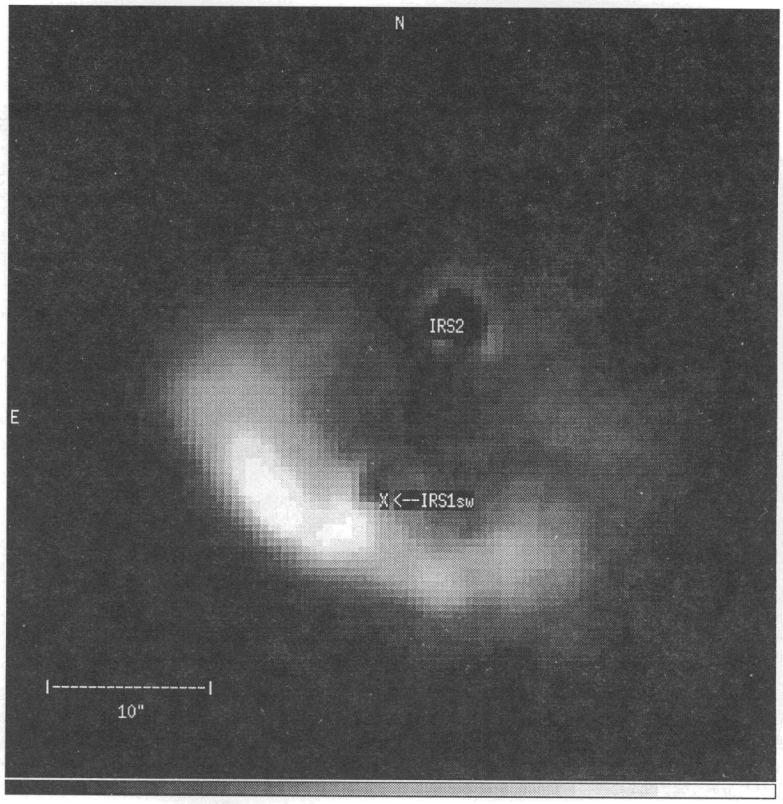

FIG. 5.—Brγ ($n = 7 \rightarrow 4$, 2.166 μm) line minus continuum. Because of seeing variations, IRS 2 does not subtract well in any of the line minus continuum images.

Figure 6 (Plate 24) shows the 3.29 μm dust feature emission (in green) surrounding the Brα emission (in red). The continuum image that was subtracted from the 3.29 μm image is quite similar in morphology to the L' image.

Table 2 gives the measured magnitudes at K as well as $[H-K]$ and $[K-L']$ colors for a number of point sources identified at K by Aspin et al. (1990). Their measurements are also provided for comparison. The two methods used to determine the magnitudes, a point spread function (psf) fit and a 5″ aperture measurement (see Table 2), bracket Aspin et al.'s measurements in most cases. Aspin et al. estimated a value of the sky and surrounding nebulosity using a concentric annulus and subtracted this off (C. Aspin, private communication). Our 5″ aperture measurements do not subtract off the surrounding nebulosity; however, the difference between the psf fit and the aperture measurements provides an estimate of the included nebulosity.

3. BRACKETT-LINE IMAGES

3.1. *Morphology*

The morphology of the Brα image and high resolution radio images (see Fig. 1 of Massi et al. 1985) of the ionized gas is essentially the same, indicating that patchy extinction, if present, is not of sufficient magnitude to seriously affect the Brα image. The morphology of the Brγ image is, on the other hand, substantially different. The peak Brγ emission has shifted substantially to the east and north of the peak at Brα and radio wavelengths, and there is a marked change in the overall shape of the emission, especially along the southwestern edge of the emission. This indicates a region of heavy 2.17 μm extinction, as we shall see later.

Maissi et al. (1985) interpret the shape of the H II region as a "blister" on the far side of the molecular cloud. When IRS 1_{sw} formed near the surface of the cloud, the surrounding gas was ionized by the star, forming a "blister" on the edge of the molecular cloud. The ionized gas then expanded past the molecular cloud boundary, into the lower density intercloud medium. This created the diffuse component of the H II region seen by Downes et al. (1975). As a cavity formed, the drop in density caused the ionization front to advance into the cloud giving rise to a dense, shell-like ionization front (see Massi et al. 1985, Fig. 1).

3.2. *Comparison with Radio*

For a region with no extinction, the Brα and Brγ line fluxes are given by the following equations (Herter 1981; Herter et al. 1981):

$$F^p_{\mathrm{Br}\alpha} = 3.2 \times 10^{-11}\, S_\nu\,(\mathrm{Jy}) \left(\frac{\nu}{5\ \mathrm{GHz}}\right)^{0.1} \times \left(\frac{T_e}{7500\ \mathrm{K}}\right)^{-0.85} \mathrm{ergs\ cm^{-2}\ s^{-1}} \quad (1)$$

$$F^p_{\mathrm{Br}\gamma} = 1.1 \times 10^{-11}\, S_\nu\,(\mathrm{Jy}) \left(\frac{\nu}{5\ \mathrm{GHz}}\right)^{0.1} \times \left(\frac{T_e}{7500\ \mathrm{K}}\right)^{-0.75} \mathrm{ergs\ cm^{-2}\ s^{-1}}, \quad (2)$$

where S_ν is the optically thin radio flux in Jy and T_e is the electron temperature. By comparing the predicted values of the Brα and Brγ fluxes with the observed values, one can then

PLATE 24

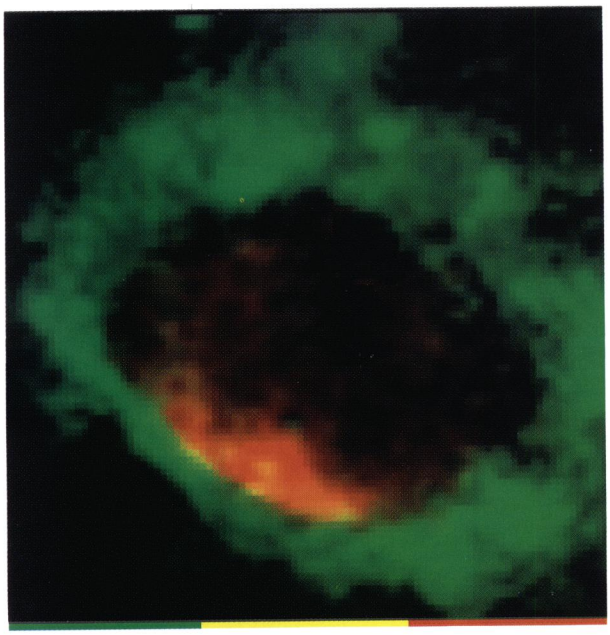

FIG. 6

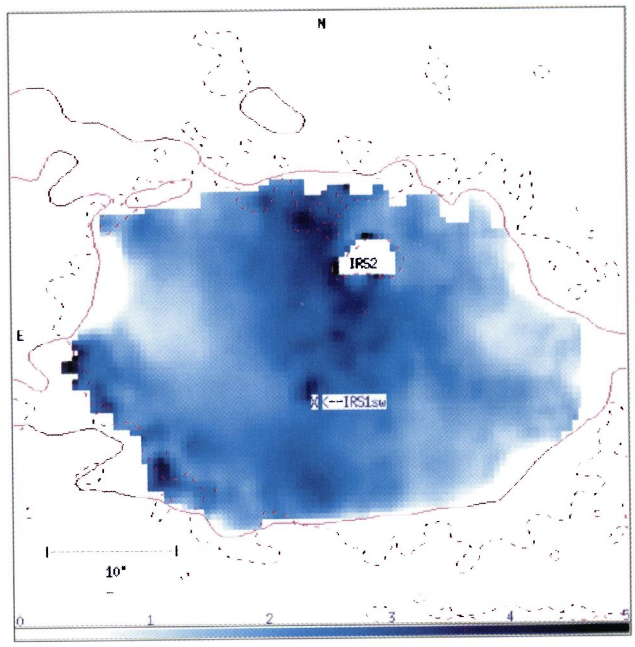

FIG. 10

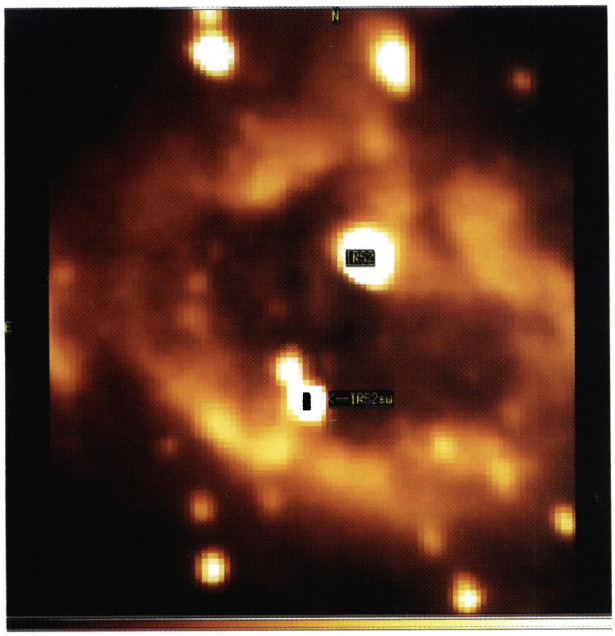

FIG. 12

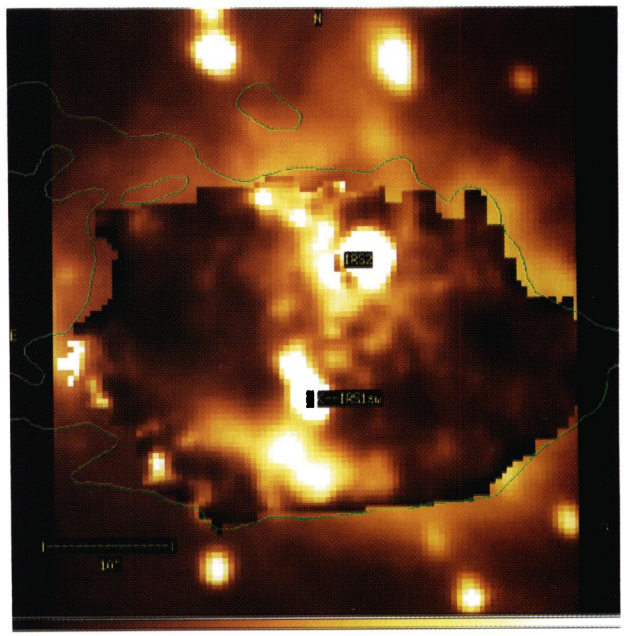

FIG. 13

FIG. 6.—3.29 μm emission in green overlaid on the Brα emission in red. The continuum has been subtracted from both. Because of seeing variations, IRS2 does not subtract well in any of the line minus continuum images.

FIG. 10.—Dust extinction optical depth at Brγ (2.167 μm) scaled from 0 to 5 on a linear scale. The image is overlaid with 3 σ contours from the Brγ (*solid line*) and 5 GHz (*dashed line*) images.

FIG. 12.—Uncorrected image at K (2.2 μm) scaled to the size of Fig. 13

FIG. 13.—Dereddened image at K (2.2 μm). The image is overlaid with the 5 GHz 3 σ contour. Inside the contour, the image has been corrected by an image of dust extinction optical depth. Outside the contour, the image is being corrected by a constant value near the average of the internal area. The area near and including IRS 2 did not subtract well in the Brγ image and is thus not being correctly dereddened (see contours on Fig. 10).

TABLE 2

K (2.2 μm), H (1.65 μm), AND L' (3.81 μm) MAGNITUDES OF POINT SOURCES IN MON R2 AS MEASURED IN 5″ SOFTWARE APERTURES

Source	Offsets from IRS 1_{SW} at K (East, North)	K mag psf fit[a]	K mag 5″ aperture	K mag Aspin[b]	$[H-K]$ color	$[K-L']$ color
IRS 1_{NE}	1″.3, 2″.3	11.84	10.29[c]	11.17	0.09	...
IRS 1_{SW}	0.0, 0.0	10.53	9.97[c]	10.08	2.48	2.88
IRS 2	−5.9, 11.3	8.84	8.60[c]	8.26	6.02	5.85
IRS 3[e]	...	...	...	6.81	...	...
IRS 4_N[f]	−12.3, −16.1	12.70	11.06[c]	12.38	1.59	2.05[d]
IRS 4_S[f]	...	12.83	...	...	0.56	...
IRS 5_N[f]	...	11.82	...	...	2.97	...
IRS 5_S[f]	−6.8, 26.6	11.82	10.35[c]	11.01	2.97	4.52
IRS 6	−7.8, −28.8	9.98	9.93	9.94	1.31	...
IRS 7	14.0, −30.1	11.58	11.28	11.84	0.93	...
IRS 9	1.8, 46.3	9.72	9.49	...	1.54	2.31
a_N	7.8, 30.6	12.13	10.83[c]	11.48	1.60	...
a_S	7.3, 27.3	10.71	10.07[c]	9.89	2.83	2.83
b_N[f]	...	13.13[c]	...	...	0.24	...
b_S[f]	7.5, −13.5	12.32	11.12[c]	11.85	2.01	2.49[d]
c_N	−0.7, 40.6	12.29	11.24[c]	...	1.23	1.95[d]
c_S	−0.6, 39.1	12.91	11.30[c]	12.0	1.38	...
d_N[f]	...	12.75	...	...	0.51	...
d_S[f]	−37.1, 14.0	12.57	11.42	12.11	1.64	1.97[d]
e	29.3, 33.1	12.81	11.79[c]	12.73	2.95	3.23[d]
f	29.3, 24.3	12.48	11.36[c]	12.82	0.41	...
g	16.3, 32.9	12.75	11.81[c]	13.29	1.41	1.58[d]

[a] A psf fit means that a point source in a 5″ aperture was scaled and then subtracted from the object in order to not include surrounding background emission. All K and H measurements were made in this fashion. All L' measurements were made directly, using 5″ software apertures, except IRS 1_{SW}, IRS 2, IRS 9, and "e," which used a psf fit. There is less extended emission at L', and measurements made in a 5″ beam differed little from using a psf fit.

[b] Aspin et al. 1990 measurements, using 5″ software apertures. Object IRS 9 was outside the Aspin et al. 1990 map. Object "c" was either not resolved into two sources, or c_N was outside the Aspin et al. 1990 map.

[c] May contain a substantial contribution from diffuse emission.

[d] We estimate ~20% uncertainty in the L' measurements of these sources.

[e] IRS 3 was saturated in all of our images.

[f] These objects are not pointlike, but were also not resolved into more than one source at H and K. Each object was fit by subtracting two separate point sources. Measurements for both components are reported.

determine the amount of extinction to the region from

$$F_\lambda^{\text{observed}} = F_\lambda^{\text{predicted}}\, e^{-\tau_\lambda}\,. \tag{3}$$

These relations assume case B recombination, optically thin Brackett line and radio emission ($\tau_{5\ \text{GHz}} = 0.15$; Downes et al. 1975), and that no He^{++} is present. The electron temperature, determined from the ratio of the H109α recombination line to the continuum (Downes et al. (1975) is 7600 ± 1200 K. Note that the dependence of the ratio of $F^P(\text{Br}\gamma)/F^P(\text{Br}\alpha)$ on the electron temperature is very weak.

Figures 7, 8, and 9 present a comparison of our Brα, Brγ, and ratio (Brγ/Brα) measurements with those of Natta et al.(1986) in 4″, 8″.5, 11″. and 20″ apertures (our apertures are synthetic software apertures). The 4″ and 8″.5 aperture measurements of Natta et al. include a correction due to the fact that their chopper throw was less than the source diameter.

M. Felli, one of the authors of Massi et al. (1985), kindly provided us with the digitized 5 GHz data presented in that paper so that we could make a detailed comparison of the Brackett line emission data to the radio data. Assuming a constant electron temperature for the region (7600 K), the 5 GHz map was used to generate a map of the optical depth, $\tau_{5\ \text{GHz}}$ and from them a map of the equivalent optically thin (eot) 5 GHz flux density. Table 3 presents a comparison of our eot radio flux density measurements using software apertures to measurements by Natta et al. (1986). Using the eot 5 GHz map with the Brα and Brγ images, τ_α and τ_γ images were then generated.

Assuming a power law dependence of extinction on wavelength, $\tau_\lambda \propto \lambda^{-\alpha}$, we use these images of τ_α and τ_γ to deduce the power-law exponent, α. A power-law index of ~1.2 ± 0.2 is found in most regions, while a power-law index of ~1.6 ± 0.1

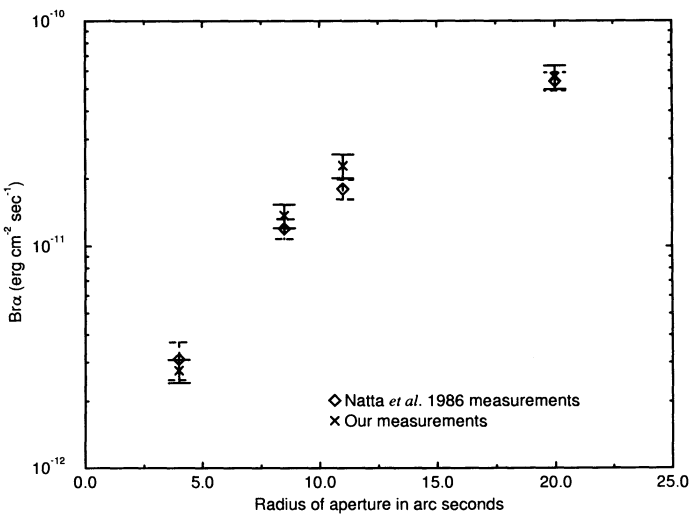

FIG. 7.—Comparison of Brα measurements (see text)

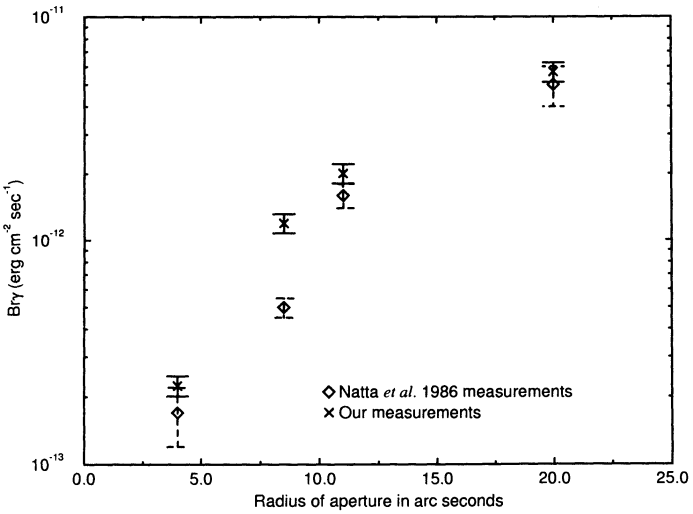

FIG. 8.—Comparison of Brγ measurements (see text)

is found near the southern knot of extinction below IRS 1_{SW}. We shall adopt a value of 1.4 as a compromise, consistent with Natta et al. (1986).

An extinction power-law index of $\alpha \sim 1.4$ is substantially flatter than the value of ~ 1.8 deduced from a compilation of extinction data for the interstellar medium (Martin & Whittet 1990; Draine 1988; Cardelli et al. 1989); Rieke & Lebofsky's (1985) extinction data for o Sco and stars in the Galactic center give rise to an extinction power law index of ~ 1.6 (see Cardelli et al. 1989) from 0.9 to 3.5 μm. Variation in the extinction on scales smaller than our resolution (1.″5) caused by clumps of denser material can lead to a flattening of the observed extinction curve (Natta & Panagia 1984), and this may be the effect we are observing. A similar effect has been proposed to model the extinction curve in K3-50 (Natta & Panagia 1984). The grain properties of the material causing the extinction may thus be the same as those in the general interstellar medium and have an extinction law index of $\alpha \sim 1.8$, while the clumpiness of the material gives rise to an observed value of $\alpha \lesssim 1.4$ (see Natta et al. 1986; Natta & Panagia 1984). Alternatively, the dust grains in the Mon R2 region may be modified from those found in the general interstellar medium. Larger grains may be found in the dense molecular cloud, while grains more typical of the interstellar medium may be found near the stars, and the resultant extinction power law might be flatter than in the general ISM.

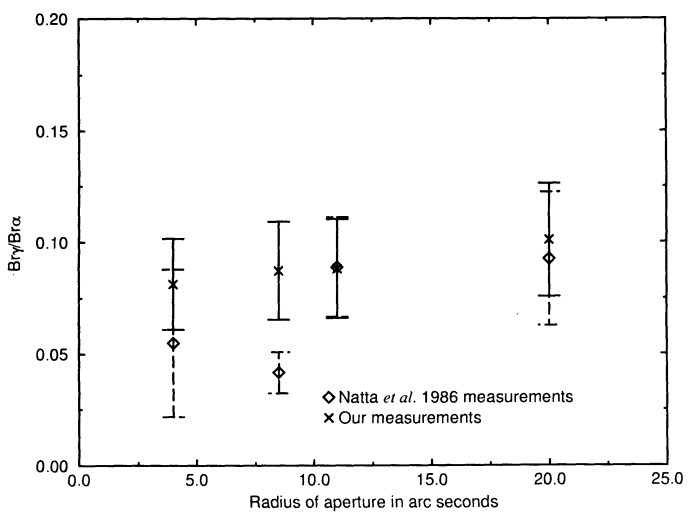

FIG. 9.—Ratio of Brγ/Brα (see text)

TABLE 3

COMPARISON OF MEASUREMENTS OF THE RADIO FLUX DENSITY IN THE 5 GHz MAP OF MASSI ET AL. 1985

Aperture Diameter	Centered on IRSI 1_{SW} (Jy)	Centered on the Radio Peak (Jy)	Natta et al. 1986 Measurements (Jy)
4″	0.30	0.50	0.96[a]
8.5	1.31	1.51	1.3
11	2.08	2.09	1.8
20	4.68	4.05	6.7
28	6.49[b]	5.61	6.7

NOTE.—Our measuremens were made using an equivalent optically thin 5 GHz map. The correction for optical depth is at most 10%.

[a] This value, as quoted in their paper, seems to be a misprint.

[b] Massi et al. 1985 report a value of 6.0 ± 1.0 Jy for the total flux density in the 5 GHz map, corresponding to 80% of the single dish value.

Smoothing the eot 5 GHz radio image, we use equation (3) to generate an image of the dust optical depth at Brγ (Fig. 10 [Pl. 24]), from which we can generate τ_λ using an extinction power law with $\alpha = 1.4$. Figure 10 shows that the extinction is patchy, with regions of higher extinction near the peak of the 5 GHz radio emission, and in the central section of the H II region surrounding IRS 2. The region of heavy extinction extending across IRS 2 to IRS 1 and west is also present in the $[H-K]$ color map (Fig. 11) as an area of redder color.

There is a finger of enhanced dust extinction extending to the southwest from IRS 2 (see Figs. 10 and 15). If the finger is modeled as a cylinder with a diameter D (along the line of sight) of 5″ (D = 5000 AU) and a length L of 10″ (across the sky) with the enhanced extinction of $\tau_v = 2$ through the center, and assuming the dust consists of low-density silicates (complex index of refraction $m = 1.5-0i$, specific density $s = 2500$ kg m^{-3}; see Whittet 1992), the density of the dust in the finger is given by

$$\rho_d \simeq 1.02 \times 10^{-26} \left\langle \frac{A_v}{D} \right\rangle_{\text{mag/kpc}} \text{(g cm}^{-3}\text{)}$$

giving $\rho_d \simeq 8.8 \times 10^{-21}$ g cm^{-3} (assuming $A_v = 10 \cdot A_\gamma$). This gives $M_{\text{dust}} \sim 4.6 \times 10^{30}$ g. If a dust to gas ratio of 0.007 (Whittet 1992) is assumed, then there is a gas mass $M_{\text{gas}} \sim 0.33$ $M_\odot$ in the finger. Alternatively, observations of the general ISM indicate that $N_H/A_v = 1.9 \times 10^{21}$ H atoms cm^{-2} (Bohlin 1975). This gives $N_H = 4 \times 10^{22}$ H atoms cm^{-2}. If we assume a diameter of 5000 AU, and a length of 10,000 AU, this gives $M_{H_2} \sim 0.38$ $M_\odot$, and $n_{H_2} = 3 \times 10^5$ cm^{-3} indicating that we are seeing stellar mass–size clumps of high-density gas. If we estimate the foreground (i.e., not due to material in the finger) extinction from the minimum extinction in the H II region, these numbers could be reduced by a factor of 2 [A_v(finger) ~ 10]. Note also that the region extending from the center of the H II region along IRS 2 to the north, and the knot to the south of IRS 1 are of even higher density ($A_v \sim 30$).

PLATE 24

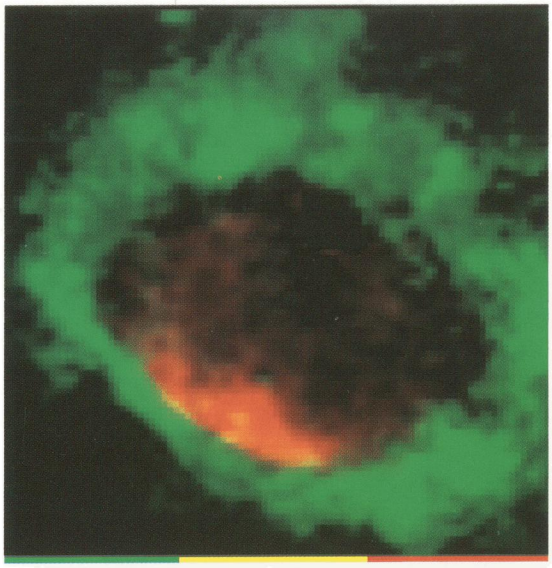

FIG. 6

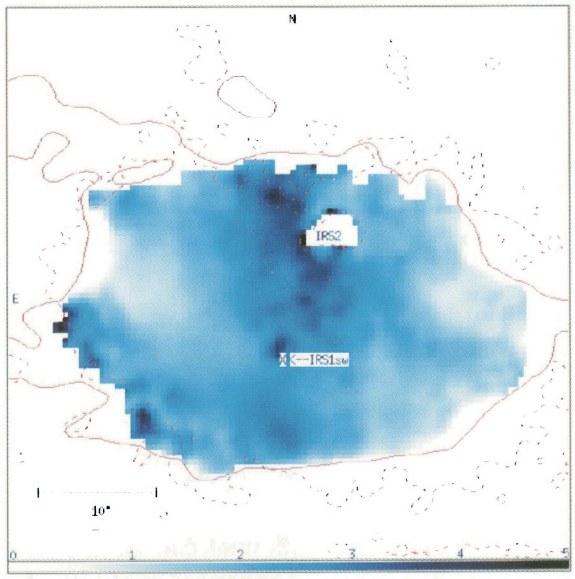

FIG. 10

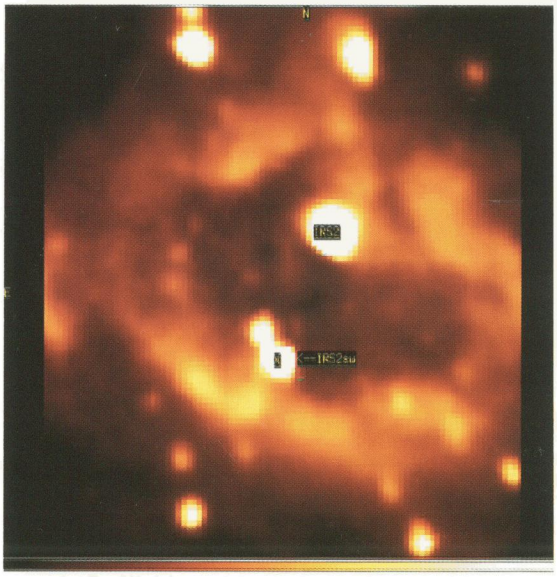

FIG. 12

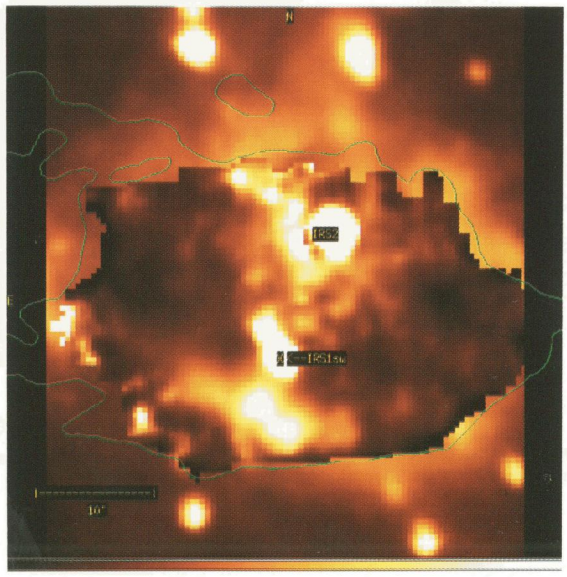

FIG. 13

FIG. 6.—3.29 μm emission in green overlaid on the Brα emission in red. The continuum has been subtracted from both. Because of seeing variations, IRS2 does not subtract well in any of the line minus continuum images.

FIG. 10.—Dust extinction optical depth at Brγ (2.167 μm) scaled from 0 to 5 on a linear scale. The image is overlaid with 3 σ contours from the Brγ (*solid line*) and 5 GHz (*dashed line*) images.

FIG. 12.—Uncorrected image at K (2.2 μm) scaled to the size of Fig. 13

FIG. 13.—Dereddened image at K (2.2 μm). The image is overlaid with the 5 GHz 3 σ contour. Inside the contour, the image has been corrected by an image of dust extinction optical depth. Outside the contour, the image is being corrected by a constant value near the average of the internal area. The area near and including IRS 2 did not subtract well in the Brγ image and is thus not being correctly dereddened (see contours on Fig. 10).

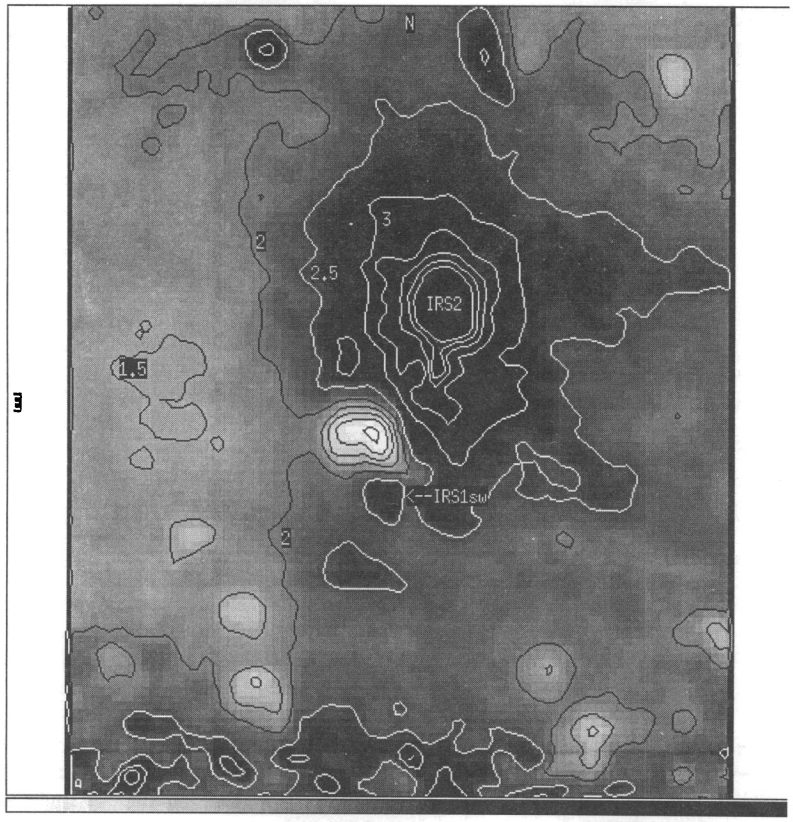

FIG. 11.—[$H-K$] color image. The image is scaled from 0 to 5 on a linear magnitude scale, with darker being "redder"; contours from 0 to 5 with an interval of 0.5 are superposed. The level 5 contour is the innermost contour around IRS 2.

4. BROAD-BAND IMAGES

4.1. *Morphology*

Our K-band and H-band images identify a large number of pointlike and extended objects as well as a shell enclosing IRS 1 and IRS 2. All of the sources identified by Aspin & Walther (1990) are present in our image except for their source h, which falls in a region not observed here.

Their naming convention will be followed except for the cases of IRS 1, and for the object they called a. Both of these objects are seen to be double. Their object IRS 1a is identified as IRS 1_{NW}, and IRS 1 as IRS 1_{SE} to more clearly indicate their relative positions. Object ai is identified as a_S and aii as a_N. In addition to these objects, object c from Aspin & Walther (1990) is seen to be double in our images. The northern and southern components are labeled c_N and c_S, respectively. There is also a source comparable in brightness to IRS 6 to the northeast of c which has been labeled IRS 9. Figure 2 has all the named sources labeled.

Aspin & Walther (1990) noted that the polarization vector pattern at K is centrosymmetric around IRS 2 with polarization reaching 45%, indicating that the IR shell is primarily right-angle scattered light originating from IRS 2 (see Aspin & Walther 1990, Fig. 4).

Comparison of H-band and K-band images shows that an apparent sheet of extinction covers IRS 2 and the northern and western parts of the IR ring. This is verified, for the region surrounding IRS 2, by the dust extinction optical depth map at Brγ (Fig. 10). The section of the ring between IRS 3 and IRS 1 is seen to be substantially brighter at H, relative to the rest of the ring, than it is at K. In fact this is the only part of the ring that appears in the 9400 Å S-1 photographs of the region (see Cohen & Frogel 1977, Pl. [5]). The line-of-sight dust extinction to the H II region (see Fig. 10) falls off toward the east side of the ring. Since the H II region is primarily within the ring, the extinction to most of the ring is not determined. Comparison of our K (2.23 μm) and H (1.65 μm) images with Figure 3 of Gonatas et al. (1992) shows lower HCO^+ emission coinciding with this section of the ring, consistent with a lower extinction, and thus bluer color.

Comparison of the H- and K-band images with the L''-band image also shows that the object IRS 2 is intrinsically very red. This is consistent with IRS 2 being a heavily enshrouded cocoon star. We assume IRS 2 is at the same distance along the line of sight as IRS 1_{SW} for the following reasons: from the polarization map IRS 2 is seen to be the source of the scattered light at 2.2 μm in the ring (see Aspin et al. 1990); the ring, seen in scattered light at 2.2 μm, is coincident with the ring of 3.29 μm emission (see Figs. 2 and 6 and § 5.2); the outer edge of the H II region is coincident with the inner edge of the ring, with some overlap; finally, the exciting source of the 3.29 μm emission is the same as that of the H II region, IRS 1_{SW}. A blackbody fit to IRS 2 (made using the $H-K$ and $K-L''$ colors, with extinction as a free parameter, contraining A_{H-K} and $A_{K-L''}$ with a $\lambda^{-\alpha}$ extinction law) indicates it has a temperature between 550 and 1200 K with a luminosity between 0.5×10^3 and 1×10^4 $L_\odot$, with a radius of $\sim$11 AU, and suffers from 25 to 60 mag of visual extinction. A luminosity of 0.5×10^4 $L_\odot$ is consistent with the pre–main-sequence phase luminosity of a 9–10 $M_\odot$ star (Iben 1965). Stahler, Palla, & Salpeter (1986) find

a luminosity of this magnitude for an 8–9 $M_\odot$ star as it enters the pre–main-sequence phase. Such an object would have a core radius of ~0.5 AU and a temperature of ~4600 K. This indicates that we are looking at a dusty shell or cocoon obscuring the central object and the cocoon reradiates the core luminosity.

Our L' image clearly shows objects IRS 1_{SW}, IRS 2, IRS 3, IRS 5, a_S, e, and IRS 9 as well as, more faintly, b, c, d and g, indicating that all of these objects are quite red. The ring is also visible as L', and its morphology is similar to that at K. There is an extension from IRS 3, pointing toward IRS 2, visible at L' but not seen at the other wavelengths we have observed. This structure is not seen in stellar calibration images.

Comparing the 9400 Å photographs of the region with an image at H shows that Cohen and Frogel's object 4 is source f; IRS 1_{NE} is object B, also seen on the Palomar Sky Survey red plate; objects 5 and 6 are most probably IRS 9 and IRS 6. There is an object on the north edge of our H image that likely corresponds to their object 1, but it is not fully in the field of view, and is missed entirely in the K image. Finally, object 3 is located near the center of IRS 3. From these comparisons, IRS 1_{NE} seems to be a foreground star and has been identified as such by Thronson et al. (1979). They find that it has the spectrum of a mid-G– to mid-K–type star. The comparisons made here also indicate that source f is a foreground star.

4.2. *Dereddening*

We now use the image of the line-of-sight extinction to the H II region, τ_γ, to generate τ_λ images. The extinction at H and at K can then be calculated for regions of overlap with the Brackett line images, assuming that the extinction is external to the emitting region. If this region is, indeed, on the back side of a molecular cloud, this is probably a reasonable assumption. Note that this assumption may not be reasonable for IRS 2, which is thought to be a cocoon star and may suffer additional local extinction if it is on the far side of the H II region. For areas outside this region, namely most of the ring and everything outside it, the extinction must be assumed. For most sources, the average extinction value found in the H II region will be applied to generate dereddened magnitudes (see Table 4 for details). The extinction to the H II region varies widely, so assuming any value outside the H II region is inherently uncertain.

Figure 13 is a dereddened image at K (see Figs. 12 and 13 [Pl. 24]). The image uses the dust extinction optical depth image (Fig. 10) to correct the central region and assumes a constant value of the dust extinction optical depth outside this region (see Fig. 13 legend). The dereddened image at H is very similar. IRS 1_{NE} is a foreground star and is therefore overcorrected for extinction. Note that most of the ring is external to the H II region and therefore outside the region being dereddened. Thus, the ring is not visible in the dereddened image except, in part, along the southeastern edge of the H II region.

From the radio flux an estimate of the amount of emission in the H and K wavelength bands due to free-free and other thermal gas emission may be made using the equations (Woodward et al. 1989)

$$F_H\ (\mathrm{Jy}) = 0.24 \cdot S_{5\ \mathrm{GHz}} \quad (5)$$

$$F_K\ (\mathrm{Jy}) = 0.26 \cdot S_{5\ \mathrm{GHz}} \quad (6)$$

for H and K, respectively. These yield, for an 8.″5 aperture, centered on the radio flux density peak [$S_{5\ \mathrm{GHz}}$(corrected) = 1.51 Jy], 0.36 Jy at H and 0.39 Jy at K, or 50% and 35% of the total, dereddened, flux at each of these wavelengths in this aperture. Since the thermal gas emission is unpolarized, this result is consistent with the lower polarization values ($\leq$12%) determined by Aspin et al. (1990) in the region of the peak

TABLE 4

CORRECTED K (2.2 μm), H (1.65 μm) AND L' (3.81 μm) MAGNITUDES

Source	H mag psf fit	K mag psf fit	L' mag	A_V (mag)	Object Type
IRS 1_{NE}	11.93	11.84	...	...	Foreground star
IRS 1_{SW}	8.84	7.80	6.36	27.3	B0–B3 star
IRS 2	10.75	6.08	1.70	27.6	Cocoon star
IRS 4_N	10.6	10.3	9.5	24	A0–B9 star
IRS 5_S	11.1	9.4	6.2	24	Nonstellar
IRS 6	7.6	7.6	...	24	B2 or foreground star
IRS 7	8.8	9.2	...	24	B4–B5 or foreground star
IRS 9	7.6	7.3	6.3	24	B1 or foreground star
a_N	10.0	9.7	...	24	B7–B8 star
a_S	9.8	8.3	6.8	24	...
b_S	10.6	9.9	8.7	24	A0–B8 star
c_N	9.8	9.9	9.2	24	B8 star
c_S	10.6	10.5	...	24	A0 star
d_S	10.5	10.2?	9.5	24	Nonstellar
e	12.1	10.4	8.5	24	...
f	12.90	12.48	...	...	Foreground star
g	10.5	10.4	10.1	24	A0 star

NOTE.—Where more than one point source was used to fit an object in Table 1, only the brighter component is reported here. All of the spectral type estimates assume a main-sequence star. Except for IRS 1, IRS 2, and f, an "average" correction was applied to each object, based on what is seen to be an average dust extinction optical depth for the H II region ($\tau_\gamma = 2.2$). IRS 1_{NE} and f are seen to be foreground objects and have no correction applied to them. IRS 1_{SW} has a correction based on a direct measurement of the extinction at its position. IRS 2 has a correction based on points in the H II region near the object, though not actually at its position. In cases where a spectral type is quoted, the H and K absolute magnitudes agreed reasonably well; however, in most of them there is seen to be an infrared excess at L'. The distance assumed for the calculation of absolute magnitudes was 950 pc.

PLATE 24

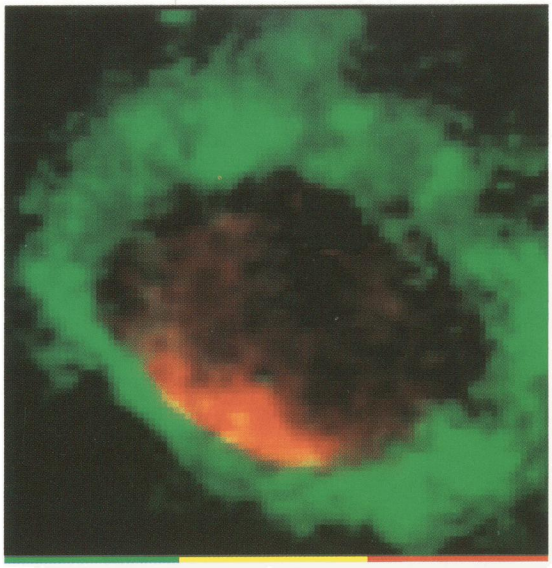

FIG. 6

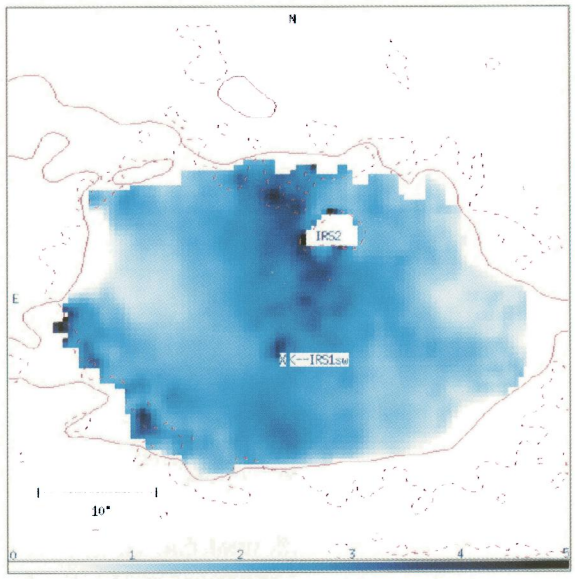

FIG. 10

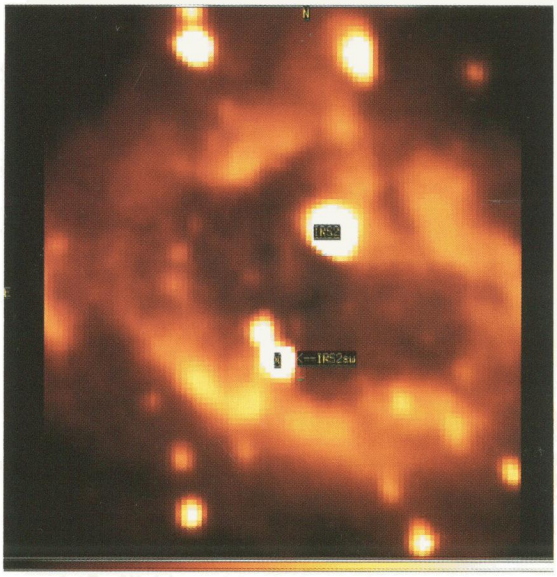

FIG. 12

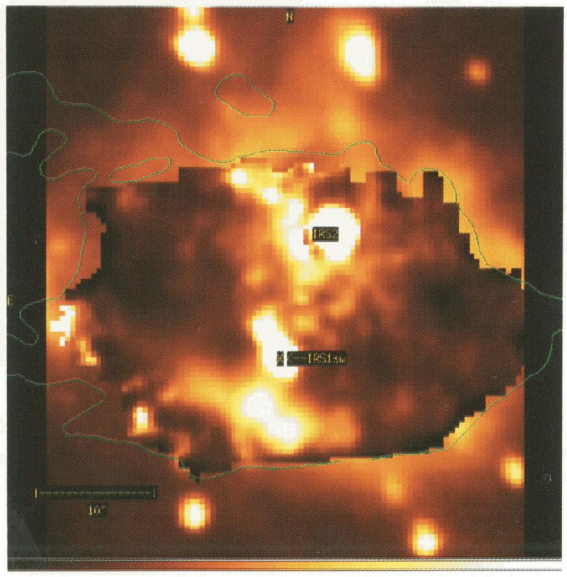

FIG. 13

FIG. 6.—3.29 μm emission in green overlaid on the Brα emission in red. The continuum has been subtracted from both. Because of seeing variations, IRS2 does not subtract well in any of the line minus continuum images.

FIG. 10.—Dust extinction optical depth at Brγ (2.167 μm) scaled from 0 to 5 on a linear scale. The image is overlaid with 3 σ contours from the Brγ (*solid line*) and 5 GHz (*dashed line*) images.

FIG. 12.—Uncorrected image at K (2.2 μm) scaled to the size of Fig. 13

FIG. 13.—Dereddened image at K (2.2 μm). The image is overlaid with the 5 GHz 3 σ contour. Inside the contour, the image has been corrected by an image of dust extinction optical depth. Outside the contour, the image is being corrected by a constant value near the average of the internal area. The area near and including IRS 2 did not subtract well in the Brγ image and is thus not being correctly dereddened (see contours on Fig. 10).

radio and Brα emission as noted previously. The polarization in other parts of the ring is ~40%. The ring is thus illuminated primarily by scattered light from IRS 2, but with an overlap of the H II region and the ring near IRS 1, a substantial fraction of the ring's illumination along the southeast rim is due to thermal gas emission. Dereddened $[H-K]$ colors at points in the ring away from the H II region overlap are also consistent with scattered light (color temperatures $\gtrsim 2000$ K).

Table 4 gives the dereddened magnitudes at H, K, and L' for a number of the sources in Table 2. Where applicable, an estimate of stellar type is given. The method used to determine the dereddening is given in the comments.

5. THREE MICRON UNIDENTIFIED EMISSION FEATURES

5.1. *Theoretical Considerations*

Emission near 3.3 μm is generally attributed to the aromatic C—H stretch mode (Duley, Williams, & Moorhouse 1991). This mode arises in both hydrogenated graphitic carbon and polycyclic aromatic hydrocarbon (PAH) molecules. Emission at 3.4 μm has been attributed to an overtone emission of the fundamental 3.29 μm feature (Barker, Allamandola, & Tielens 1987). The 3.4 μm feature is near the $v = 2 \rightarrow 1$ vibrational "hot band" transition of the C—H stretch mode in a number of PAH molecules (see Geballe et al. 1989). It has also been attributed to aliphatic C—H; carbon in this case is sp^3 bonded (Duley et al. 1991).

In the first case, smaller PAHs have fewer excitable vibrational modes and thus more frequent excitation of the $v > 1$ levels are expected. These smaller PAH molecules are also more susceptible to photodissociation by the UV field. In regions of strong UV fields, some hydrogen atoms are stripped from their carbon atom "skeleton," since the energy needed to remove a hydrogen atom is only 4.5 eV, while the energy to break off a carbon atom is significantly higher (11 eV; see Geballe et al. 1989, Table 2). Since the 3.29 and 3.4 μm emission is most likely due to a C—H stretch mode, dehydrogenated atoms will not emit. Thus, in regions with strong UV fields, PAHs below a certain size will not emit in these bands. Although larger PAH molecules will be hydrogenated, they will have little emission from the $v = 2$ or higher vibrational modes, since they have many vibrational modes. Farther from the star, the PAHs will be completely hydrogenated and the smaller PAHs will emit in the 3.4 μm band. This will give rise to an increase in the ratio of 3.4 to 3.29 μm emission with distance from the star (Geballe et al. 1989).

In the second case hydrogenated amorphous carbon (HAC) can be formed with either sp^2 or sp^3 carbon bonds. The 3.4 μm emission would then be due to aliphatic C—H (i.e., where the carbon is sp^3 bonded). Duley et al. (1991) propose the following model for HAC dust emission in a PDR: Deep in the molecular cloud the sp^2 to sp^3 ratio is of order unity. Closer in to the star, in a UV ($\lambda > 1108$ Å) intensity of χ times the interstellar value, HAC grains are graphitized in $\tau \lesssim 10^6/\chi$ yr, and the material is significantly dehydrogenated in the process. In the regions close enough to the star for H_2 to be dissociated, the graphitized carbon is subjected to a flux of H atoms, forming surface layers of H-rich polymeric (sp^3 bonded) carbon which, if shocked, may be eroded from the grains, giving rise to PAHs.

Again, the general trend is for an increase in the ratio of the 3.4 to 3.3 μm emission with distance away from the star into the molecular cloud. However, in the H I and H II regions, where the graphitized carbon is being subjected to a significant flux of H atoms, the relative strengths of the 3.4 and 3.3 μm emission bands are determined by the ratio of H-atom density to UV flux. In either case if the UV intensity is high enough, all molecules will be dissociated, and no emission will be seen.

5.2. *Observations*

Figure 6 shows that 3.29 μm emission is predominately confined to the location of the ring, seen in scattered light at K. The emission at 3.4 μm is of lower signal-to-noise ratio ratio (~2–3 rather than 10 for the 3.29 μm emission); however, the same ring structure is also seen.

Since the wavelengths involved are very close together, the difference in extinction between these two emission features is negligible. Comparing the relative strengths of the 3.4 and 3.29 μm features, as a function of distance from IRS 1_{SW}, may give some information on the emitting populations. The low signal-to-noise ratio of the 3.4 μm image renders our use of this technique uncertain, however.

The 3.4 to 3.29 μm flux ratio is higher (~0.2 to 0.4 as compared to ~0.05 to 0.1 in the rest of the ring) in a small bar running from directly south of IRS 1_{SW} to the eastnortheast, for ~5″. This may indicate that there is an enhancement of 3.4 μm emission very close to the exciting star of the H II region. Unless this bar is not in the same plane as the ring, this finding contradicts that of Geballe et al. (1989). The ratio is also higher in the region of the ring directly northeast of IRS 2, perhaps indicating an enhancement of the 3.4 μm emission moving away from IRS 1_{SW}. However, this enhancement is not uniform and is not seen moving away from IRS 1_{SW} in other parts of the ring.

Over the whole ring region, there is no general trend detected for either an enhancement or a reduction of 3.4 μm emission relative to 3.29 μm emission. This indicates that the populations emitting at 3.4 and 3.29 μm are either the same, or well intermixed, and the ratio of H-atom flux to UV field is relatively constant over this region. The unidentified feature emission also traces out the 2.2 μm ring very closely, indicating that the dust scattering light from IRS 2 at 2.2 μm is found in approximately the same location as the material emitting in the 3 μm emission bands. Higher signal-to-noise ratio observations of the 3.4 μm emission band are required to determine if there is indeed any variation in the ratio of the 3.29 μm emission in Mon R2.

The 3.29 and 3.4 μm emission falls along and outside the outer edge of the H II region, as traced out by Brα, in most parts of the ring (see Fig. 6). However, this emission overlaps the H II region along the brightest part of the Brα emission, the southeast part of the ring. The reason for the overlap along the southeast edge of the H II region is, most likely, a density enhancement effect, or a projection effect. If it is a density enhancement effect, an increase in the H-atom density will balance out the dehydrogenation of the PAH molecules by the UV radiation field, by increasing the likelihood of collisions between the carbon "skeletons" and the free-floating H atoms. This density enhancement is consistent with the "blister model" of Massi et al. (1985) previously discussed.

In NGC 7027 Woodward (1987) found that a significant fraction of the 3.29 μm emission present in this object must arise interior to the H II region, though ≥60% of the features arise from a thin shell just outside the ionized zone. This indicates that, under at least some physical conditions, the material emitting at 3.29 μm is robust enough to survive a hard UV radiation field for a period of time.

6. DISCUSSION

In the previous sections, we have shown that a number of the features of the near infrared emission from Mon R2 IRS seem to be consistent with the "blister model" of Massi et al (1985). In order to provide a coherent picture of this region, it is necessary to explain the larger scale structure and outflow as well as the near-infrared emission and to adapt the blister model to this larger picture.

There is a massive CO outflow centered on Mon R2 IRS and extending roughly northwest (blueshifted emission) to southeast (redshifted emission) for 28′ (Wolf et al. 1990). There is also a region of dense molecular gas traced out in CS (Wolf et al. 1990) and HCO^+ (Gonatas et al. 1992), running perpendicular to the CO outflow.

The magnetic field lines, as traced out by *I*-band polarization (Hodapp 1987) run along the direction of CO outflow, and thus, perpendicular to the HCO^+ and CS elongation. This is consistent with a cloud collapsing preferentially along the magnetic field lines (see also Loren 1977). The CS observations (Wolf et al. 1990) indicate an overall rotation of the dense material. The northeastern lobe of material seen in HCO^+ is seen to be redshifted, while the southwestern lobe is blueshifted. Gonatas et al. (1992) claim that the transition from one lobe to the other is too abrupt to be caused by rotation; however, the central region of the HCO^+ emission is seen to be evacuated, and thus an abrupt transition in velocity is what would be expected, due to the abrupt density change. The energetics of the outflow are strong enough to have disrupted the gravitational binding of the dense core region (see Wolf et al. 1990); thus it may be that overall cloud rotation has been turbulently disrupted.

Gonatas et al (1992) show that there is a region of lower intensity emission in the HCO^+ emission coincident with the location of the H II region. The HCO^+ emission is found in two dense lobes to the northeast and to the southwest of the H II region.They argue that if the region of the enhanced H II emission, along the southeastern section of the ring, is due to dense material blocking the expansion of the hot gas, they would expect stronger HCO^+ emission from this region, rather than less as is seen, and that the H II region may have already blown away most of the molecular material in this direction.

We propose the following modification of the blister model: if the HCO^+ is found in a torus tilted between 45° and 90° to the line of sight, with the northwest side being nearer to us, and the axis of symmetry running in a northwest to southeast direction see (Fig. 14), a lobe structure would be seen due to the increase in column density through the molecular material in the northeast and southwest parts of the torus. The ridge of emission seen in the radio and in the Brackett lines is identified with ionization of the inner edge of the torus. The fact that the ionizing star is not located in the center of the torus but offset to the southeast then explains the ridge of emission seen at 5 GHz and in the Brackett lines. The lower HCO^+ emission along the ridge is then due to a shorter pathlength through this

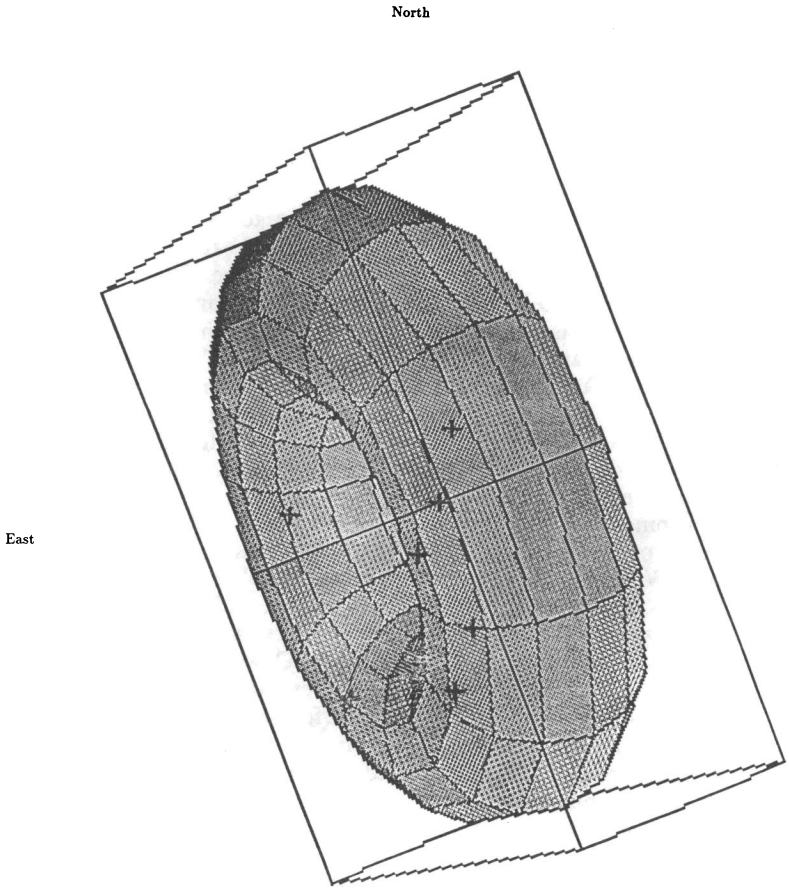

FIG. 14.—Cartoon of "Torus model." Positions of IRS 1–7 are indicated by plus signs on the figure.

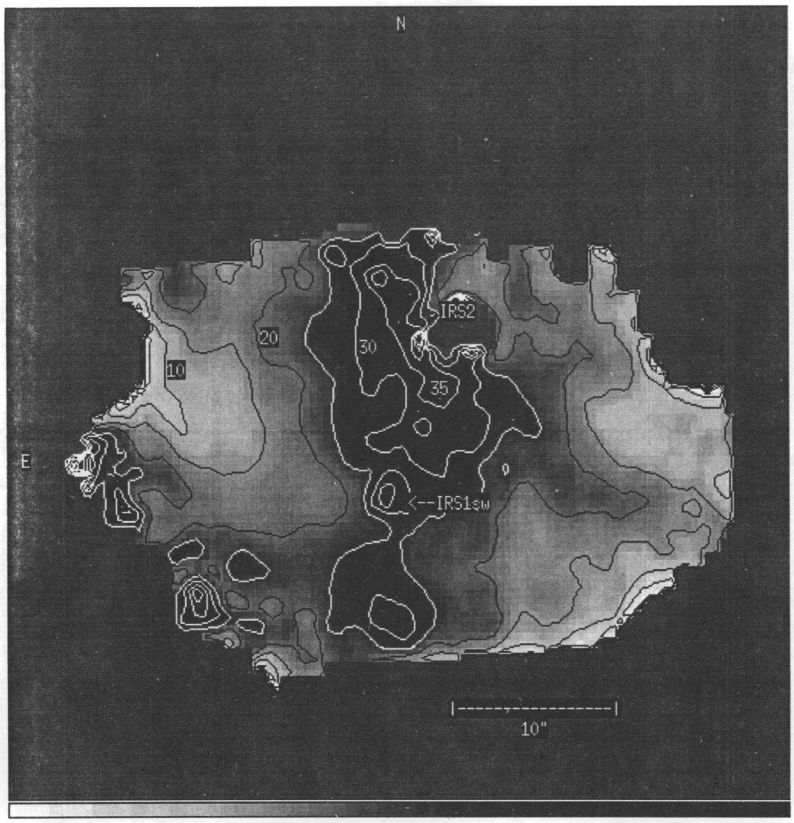

FIG. 15.—Gray-scale image of A_V displayed on a linear magnitude scale from 0 (white) to 40 (black. The image is overlaid with contours in steps of 5 magns. A_V is assumed to be $10 \times A_K$. The 10, 20, 30, and 35 mag contours are marked on the figure. The area near and include IRS 2 did not subtract well in the Brγ image and has been replaced by an average value of the extinction assumed for the external region (see contours on Fig. 10).

part of the torus than is found in the lobes. In this picture, the model of Massi et al. (1985) is still a valid approximation. We are simply replacing their spherical shell with a more cylindrical shell in the center of the torus.

If this is indeed the case, the ring of scattered light seen at 2.2 μm is light from IRS 2 reflected off the inner edge of the torus. The geometry then explains the collimation of the CO bipolar outflow, the shape of both the HCO^+ and CS emission, and the morphologies of both the compact H II region and the dust ring seen in the broad-band and 3.29 μm near-infrared images.

7. SUMMARY

The advent of sensitive near-infrared detector arrays has given rise to a number of ways of probing star formation regions on a fine spatial scale not before possible, or possible only by painstaking mapping techniques. We have imaged the massive star formation region Mon R2 in a number of broad-band, near-infrared, wavelength bands, as well as at Brα, Brγ, and in the 3.29 and 3.4 μm unidentified emission bands.

Images of Mon R2 in the Brackett emission lines compared with radio emission images lead to an image of the small-scale line-of-sight extinction to the H II region (see Fig. 15). The wide variation in extinction across the Mon R2 compact H II region shows the inherent unreliability of assuming a constant value of extinction, based on even relatively small aperture measurements.

An adaptation of Massi et al. (1985)'s blister model is proposed to explain the larger scale CO outflow, the morphology of the dense molecular gas as traced out by HCO^+ and CS, as well as the ring seen in the near infrared. This model is one of a torus of dense gas with the H II region forming the "doughnut hole." The torus collimates the CO outflow. The ring of material visible at 2.2 μm is largely scattered light from IRS 2 off the inner edge of the torus, and the ridge of emission seen in both the radio continuum and the Brackett lines is due to the fact that the ionizing source is not at the center of the "doughnut hole," but offset to the southeast. The material emitting at 3.29 and 3.4 μm is spatially coincident with the dust scattering light at 2.2 μm, and there is no overall trend detected in variation of the 3.29 to 3.4 μm emission with projected distance from IRS 1_{SW}.

The authors wish to thank those who helped in this endeavor: J. Garnett, S. Libonate, S. Satyapal, S. Solomon, and P. Turner for helping with the various observations; S. Libonate, S. Solomon, and P. Turner for helping with various stages of the image reduction; M. Felli, for providing the digitized radio data; N. Cowen and K. McFadden for computer support; A. LaBarbera and H. van Tassell for transferring images; and R. Gehrz for time and assistance at Mount Lemmon. S. Solomon wrote the mosaicking software, and S. Libonate wrote the least-squares fitting routine used to determine the distortion and plate scale. We would also like to thank the referee, C. Aspin, for a number of helpful suggestions. The Astronomical Society of New York and the National Geographical Society provided funds for travel. The research was supported by a grant from the NSF.

REFERENCES

Aspin, C., & Walther, D. M. 1990, A&A, 235, 387
———. 1991, in Astrophysics with Infrared Arrays, ed. R. Elston (ASP Conf. Ser. 14), 288
Barker, J. R., Allamandola, L. J., & Tielens, A. G. G. M. 1987, ApJ, 315, L61
Beckwith, S., Evans, N. J., II, Becklin, E. E., & Neugebauer, G. 1976, ApJ, 208, 390
Bohlin, R. C. 1975, ApJ, 200, 402
Cardelli, J. A., Clayton, G. C., & Mathis, J. S. 1989, ApJ, 345, 245
Cohen, J. G., & Frogel, J. A. 1977, ApJ, 211, 178
Downes, D., Winnberg, A., Goss, W. M., & Johansson, L. E. G. 1975, A&A, 44, 243
Draine, B. T. 1988, unpublished
Duley, W. W., Williams, D. A., & Moorhouse, A. 1991, MNRAS, 253, 505
Geballe, T. R., Tielens, A. G. G. M., Allamandola, L. J., Moorhouse, A., & Brand, P. W. J. L. 1989, ApJ, 341, 278
Gonatas, C. P., Palmer, P., & Novak, G. 1992, ApJ, 398, 118
Herter, T. 1981, Ph.D. thesis, Univ. of Rochester
Herter, T., et al. 1981, ApJ, 250, 186
Hodapp, K. W. 1987, A&A, 172, 304
Iben, I., Jr. 1965, ApJ, 141, 993
Loren, R. B. 1977, ApJ, 215, 129
Martin, P. G., & Whittet, D. C. B. 1990, ApJ, 357, 113
Massi, M., Felli, M., & Simon, M. 1985, A&A, 152, 387
Natta, A., Beckwith, S., Evans, N. J., II, Beck, S. C., Moorwood, A. F. M., & Oliva, E. 1986, A&A, 158, 143
Natta, A., & Panagia, N. 1984, ApJ, 287, 228
Rieke, G. H., & Lebofsky, M. J. 1985, ApJ, 288, 618
Stahler, S. W., Palla, F., & Salpeter, E. E. 1986, ApJ, 302, 590
Thronson, H. A., Jr., Gatley, I., Harvey, P. M., Sellgren, K., & Werner, M. W. 1980, ApJ, 237, 66
van den Bergh, S. 1966, AJ, 71, 990
Whittet, D. C. B. 1992, Dust in the Galactic Environment (Bristol: Institute of Physics)
Wolf, G. A., Lada, C. J., & Bally, J. 1990, AJ, 100, 1892
Woodward, C. 1987, Ph.D. thesis, Univ. of Rochester
Woodward, C. E., Pipher, J. L., Shure, M., & Forrest, W. J. 1989, ApJ, 342, 860